A Comprehensive Analysis of Laser-Induced Ignition of RDX Monopropellant

Y.-C. LIAU
Chemical Science and Technology Division, Los Alamos National Laboratory, Los Alamos, NM 87545, USA

and

E. S. KIM and V. YANG*
Department of Mechanical and Nuclear Engineering, The Pennsylvania State University, 104 Research Building East, University Park, PA 16802, USA

A comprehensive analysis of laser-induced ignition of 1,3,5-trinitrohexahydro-s-triazine (RDX) monopropellant has been performed with consideration of detailed chemical kinetics. The model considers the transient development in the entire combustion zone, including the solid-phase, subsurface two-phase, and gas-phase regions. The formulation accommodates detailed chemical kinetics and transport phenomena in the gas phase, as well as thermal decomposition and subsequent reactions in the subsurface two-phase region. Thermodynamic phase transition and volumetric radiant energy absorption are also considered for completeness. The analysis is capable of treating the complete ignition process from surface pyrolysis to steady-state combustion, with the instantaneous burning rate and surface conditions treated as part of the solutions. Numerical experiments were conducted at atmospheric pressure in argon with CO_2 laser heat flux from 35 to 600 W/cm^2. Excellent agreement was obtained between the calculated and measured ignition delays. The propellant gasification rate increases with increasing laser intensity, which in turn shortens the ignition delay. The entire process can be divided into six stages: inert heating, thermal decomposition, occurrence of primary flame, preparation and formation of secondary flame and, finally, establishment of steady-state combustion. The major process in the primary flame is identified as the consumption of CH_2O, HONO, NO_2, H_2CN, H_2CNNO_2, and HNO. In the secondary flame, the conversion of NO and HCN to N_2, CO, H_2O, and H_2 is the key exothermic process causing ignition in the gas phase. © 2001 by The Combustion Institute

NOMENCLATURE

A	cross-sectional area of propellant sample
A_j	pre-exponential factor of rate constant of jth reaction
A_{sp}	specific surface area
B_j	temperature exponent in rate constant of jth reaction
C_i	molar concentration of ith species
$\dot{C}_{ij}$	rate of change in molar concentration of ith species by jth reaction
$c_{\mathrm{p}i}$	constant pressure heat capacity of ith species
D_i	effective mass-diffusion coefficient of ith species
D_{T_i}	thermal diffusion ratio of ith species
E_j	activation energy of jth reaction
e	internal energy
f_{g}	fraction of laser energy absorbed by gas phase
H_{fus}	molar heat of fusion
H_{sub}	molar heat of sublimation
H_{v}	molar heat of evaporation
h	enthalpy
h_i	enthalpy of ith species
$h^\circ_{\mathrm{f}i}$	heat of formation of ith species at standard condition
k_j	rate constant of jth reaction
m''	mass flux
N	total number of species
N_{R}	total number of reactions
P	pressure
$P_{\mathrm{v,eq}}$	equilibrium vapor pressure of RDX
$\dot{Q}''_{\mathrm{laser}}$	external laser heat flux
$\dot{Q}'''_{\mathrm{rad}}$	volumetric absorption of laser energy
R_u	universal gas constant
s	sticking coefficient
T	temperature
t	time
u	bulk velocity
V_{cor}	correction velocity
V_i	diffusion velocity of ith species
W_i	molecular weight of ith species
$\dot{w}_i$	mass production rate of ith species

---

* Corresponding author. E-mail: vigor@psu.edu

0010-2180/01/$–see front matter
PII S0010-2180(01)00281-4

COMBUSTION AND FLAME 126:1680–1698 (2001)

Published by Elsevier Science Inc.

$\dot{w}_{Rj}$	mass production rate of *j*th reaction
X_i	mole fraction of *i*th species
x	spatial coordinate
Y_i	mass fraction of *i*th species

Greek Symbols

β	absorption coefficient
κ_i	absorption cross-section of *i*th species
ϕ	void fraction
ρ	density
λ	thermal conductivity
$\dot{\omega}$	molar production rate

Subscripts

0^+	gas-phase side of propellant surface
0^-	subsurface side of propellant surface
bw	backward reaction
c	condensed phase
fw	forward reaction
g	gas phase
id	ignition delay
ini	initial condition
l	liquid phase
l→g	from liquid to gas
m	melting
net	net value of evaporation rate minus condensation rate
s	solid phase
sur	surface
t	mass-averaged quantity in two-phase region
v	vapor

INTRODUCTION

Ignition of solid propellants and explosives involves an array of intricate physiochemical processes under energetic stimuli, and has been a subject of extensive research since 1950. A comprehensive review of the early work was conducted by Price et al. in 1966 [1]. The experimental and theoretical literature pertaining to the ignition of solid propellants over the period of 1966 through 1980 was reviewed by Kulkarni et al. [2] and Hermance [3]. The state of understanding in Russia up to 1989 was presented by Vilyunov and Zarko [4], giving a detailed examination of the various ignition models and related experimental approaches. Recently, a review of laser and radiative ignition of 24 solid energetic materials, with emphasis on work performed in the former Soviet Union, was provided by Strakouskiy et al. [5].

As shown in Table 1, many theoretical models have been developed to study the ignition of solid propellants and explosives, which can be broadly divided into three categories: solid-phase (or reactive solid), heterogeneous, and gas-phase reaction models. The solid-phase reaction models [6–9] assume that exothermic reactions in the condensed phase are the dominant mechanism of ignition, whereas the effects of surface and gas-phase processes are secondary and can be neglected. The formulation usually includes the energy equation for the condensed phase, with the species-concentration equations treated as optional. The convection terms are often ignored for simplicity. Ignition criteria are defined based on conditions at which thermal run-away or steady-state combustion takes place. Primary results include: 1) ignition delays as functions of condensed-phase reaction parameters, external heat flux, ambient pressure, and propellant preconditioned temperature, among others; and 2) evolution of the temperature field in the regime of interest. Due to the basic assumptions employed, this type of model is suitable for materials in which condensed-phase heat release represents the rate-controlling step in determining the propellant burning behavior, such as double-based propellants. The pressure dependence of ignition delay, however, is commonly underestimated because the condensed-phase process is insensitive to pressure.

Heterogeneous reaction models [10–18] assume that heterogeneous reactions at the propellant surface are responsible for ignition due to the molecular diffusion of ambient oxidizer species to the propellant surface. The formulation takes into account the condensed-phase conservation equations of energy and species concentration along with interfacial boundary conditions. A number of ignition criteria, such as go/no-go, pre-specified flame and surface temperatures, and temperature gradient have been used. As anticipated, results indicate that the activation energies of surface heterogeneous reactions have strong influences on ignition delay and temperature evolution in the

TABLE 1

Theoretical Models of Solid-Propellant Ignition

	Solid-phase reaction models	Heterogeneous reaction models	Gas-phase reaction models
Presumption	Solid-phase reactions cause ignition.	Heterogeneous reactions at surface cause ignition.	Gas-phase reactions cause ignition.
Primary concern	Condensed phase.	Condensed phase and interface.	Gas phase and condensed phase.
Formulation	Energy eq. for condensed phase. Species eqs. for condensed phase (optional). Convection terms are usually neglected in analytical approach.	Energy eq. for condensed phase. Species eqs. for condensed phase (optional). Convection terms are usually neglected in analytical approach.	Energy eqs. for both phases. Species eqs. for gas phase. Species eqs. for condensed phase (optional). In-depth radiation absorption is usually neglected.
Approach	Asymptotic method. Numerical method.	Laplace transform. Local similarity. Asymptotic method. Classical thermal theory. Numerical method.	Numerical method. Asymptotic method.
Ignition criteria	Go/No-Go. $T/T_{\mathrm{ref}} \to \infty$. Steady-state combustion.	Go/No-Go. $T/T_{\mathrm{ref}} \to \infty$. $dt/dT_{\mathrm{s}} \to 0$ (or $dT_{\mathrm{s}}/dt \to \infty$). T_{s} rises to specified value.	$T/T_{\mathrm{ref}} \to \infty$. T_{s}, dT_{s}/dx, Y_j, or gas reaction rate (RR) rises to specified values. Emission of light. Steady-state combustion.
Major results	Ignition delay as function of rate constant, heat flux, pressure, and others. $T(x,t)$ in the solid.	Ignition delay as function of surface reaction rate and oxidizer concentration. $T(x,t)$ in the solid and surface conditions.	Ignition delay as function of surface condition for shock tube; or heat flux and pressure for laser. $T(x,t)$ in both phases and $Y_i(x,t)$ in gas phase.
References	[6–9]	[10–18]	[19–26]
Remarks	Suitable for condensed-phase controlled materials, such as double-based propellants. Effect of pressure is underestimated since condensed-phase process is insensitive to pressure.	Suitable for the surface-reaction controlled material, such as polymers, hypergolic systems, etc. Effect of surface reaction is overestimated for solid propellants, especially for homogeneous propellants. Surface reaction with lowest activation energy dominates ignition.	Suitable for gas-phase controlled material, such as low vulnerability ammunition (LOVA) propellants. Detailed chemistry is established and ready to be employed in the model.

condensed phase. This kind of model has been widely applied to shock-tube ignition studies, and is suitable for diffusion-controlled burning materials such as carbon, polymers, etc. The effect of diffusion processes, however, is often overestimated for solid-propellant combustion.

Unlike the previous two categories, the gas-phase reaction models [19–26] presume that exothermic gas-phase reactions and their heat feedback to the propellant surface are the primary mechanism of ignition. Conservation of energy and species concentration in the gas phase is of major concern, but the condensed-phase equations are also included for completeness. In addition to the commonly used ignition criteria, emission of light and achievement of steady-state combustion are employed in some studies. Results typically include ignition delay as a function of surface condition for shock-tube cases or heat flux and pressure for radiant cases. Also included are the time evolution of the temperature fields in both phases and the species-concentration profiles in the gas phase. As a result of the basic assumptions used, the models are suitable for gas-phase controlled burning materials and have been successfully applied to several ignition problems, such as fuel in hot oxidizing gas [19, 20], homogeneous propellants under shock-tube conditions [21, 22], heterogeneous propellants in hot oxidizing gases [23], and laser-induced ignition [24–26].

In spite of their contributions in correlating experimental data and providing qualitative understanding of ignition behavior, all the existing models [6–26] are semi-empirical in nature and do not provide predictive capability at scales sufficient to resolve the detailed ignition mechanisms and flame evolution. A prior understanding of the ignition process is usually required before modeling. This obstacle mainly results from the use of global kinetics schemes derived for steady-state combustion. Moreover, a simple pyrolysis law is often employed to describe the propellant gasification process in terms of propellant surface temperature along with prescribed condensed-phase heat release. The lack of reliable thermochemical parameters poses another limitation in model accuracy.

During the past decade, a series of analyses based on detailed chemistry has been conducted to investigate 1,3,5-trinitrohexahydro-5-triazine (RDX) steady-state combustion [27–33]. Such models have successfully predicted the entire combustion-wave structure and propellant burning rate over a broad range of ambient conditions. The present work attempts to establish a general framework for studying the key physiochemical processes involved in the laser-induced ignition and combustion of RDX monopropellant. The analysis extends the steady-state model described in [29, 30] to include the transient development in the entire combustion zone, including the solid-phase, near-surface two-phase, and gas-phase regions. The formulation accommodates detailed chemical kinetics and transport phenomena in the gas-phase region, as well as thermal decomposition and subsequent reactions in the two-phase region. Thermodynamic phase transition and volumetric radiant energy absorption are also considered for a complete description. The model is capable of treating the entire ignition process from surface pyrolysis to steady-state combustion, with the instantaneous burning rate and surface conditions treated as part of the solution.

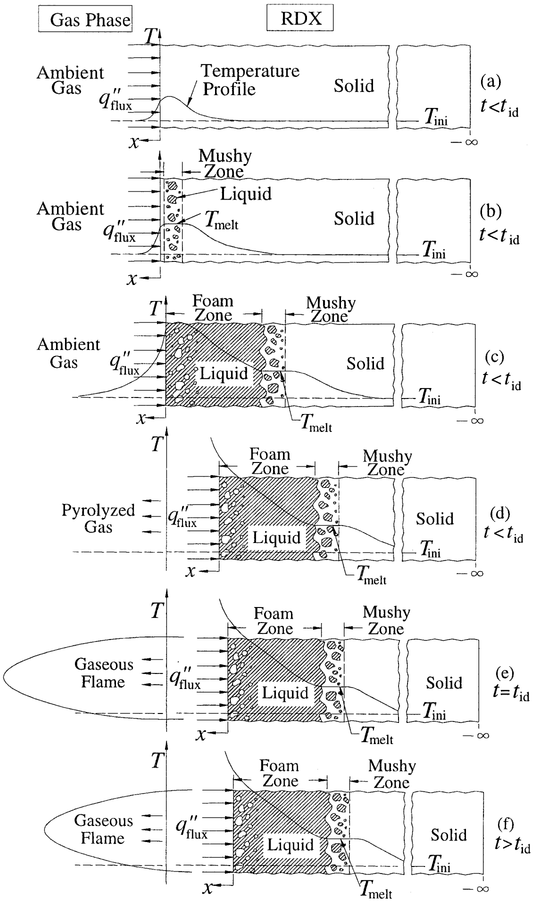

Fig. 1. Physiochemical processes involved in laser-induced ignition of RDX.

The paper is organized as follows. A theoretical formulation of RDX ignition is first described, and then the numerical technique used in this work is discussed briefly. The entire laser-induced ignition process of RDX is then examined in depth. Special attention is given to the ignition delay and key physiochemical processes responsible for achieving ignition.

THEORETICAL FORMULATION

The physical problem of concern is the ignition of a strand of RDX monopropellant induced by a continuous and radially uniform CO_2 laser. The detailed physiochemical processes involved are schematically illustrated in Fig. 1. The propellant and the ambient gas are initially at room temperature. Once the laser is activated, volumetric absorption of laser energy in the solid phase takes place, as shown in Fig. 1a. In the gas phase only certain gaseous species, such as vapor RDX, absorbs a noticeable amount of laser energy at the wavelength of 10.6 μm; thus, the gas-phase absorption is negligible during the inert heating period. When the solid reaches its melting temperature, the absorbed radiant energy cannot further raise the temperature without first melting the solid. Because the radiant energy absorbed is insufficient for instantaneous melting of all of the solid in a short period, partial melting of the solid occurs, which leads to the formation of a mushy zone that consists of both solid and liquid (Fig 1b). When a pure liquid layer is formed, the solid–liquid interface starts to move due to conductive and radiative heat transfer (Fig. 1c). In the liquid, thermal decomposition and subsequent reactions, as well as phase transition, take place, generating gas bubbles and forming a two-phase region. The propellant then undergoes a sequence of rapid evaporation at the surface (Fig. 1d). Ignition occurs if the heat flux is sufficiently large to initiate the subsequent self-accelerated exothermic reactions that result in substantial heat release (in the gas phase) and emission of light. A luminous flame is produced, regresses toward the surface, and finally reaches a stationary position corresponding to its steady-state condition.

The present work extends the analysis previously developed for the steady-state combustion of RDX [29, 30] to include the transient development during the entire ignition process. A brief description of the theoretical model is given below, with detailed information available in [30, 34].

Gas-Phase Processes

The formulation for the gas-phase region is based on the mass, energy, and species transport for a multi-component chemically reacting system of N species, and accommodates finite-rate chemical kinetics and variable thermophysical properties. If body force, viscous dissipation, and kinetic energy are ignored, the conservation equations for an isobaric flow can be written as follows.

Mass

$$\frac{\partial(\rho A)}{\partial t} + \frac{\partial}{\partial x}(\rho u A) = 0 \tag{1}$$

Species concentration

$$\rho A \frac{\partial Y_i}{\partial t} + \rho u A \frac{\partial Y_i}{\partial x} + \frac{\partial}{\partial x}(\rho A V_i Y_i) = A \dot{w}_i \qquad (i = 1, 2, \ldots, N) \tag{2}$$

Energy

$$\rho c_p A \frac{\partial T}{\partial t} - \frac{\partial(pA)}{\partial t} + \rho u c_p A \frac{\partial T}{\partial x} = \frac{\partial}{\partial x}\left(\lambda A \frac{\partial T}{\partial x}\right) - A \sum_{i=1}^{N}\left(\rho Y_i V_i c_{p_i} \frac{\partial T}{\partial x} + \dot{w}_i h_i\right) + A \dot{Q}'''_{\mathrm{rad,g}} \tag{3}$$

where subscript i denotes the ith species. The specific enthalpy h_i is defined by:

$$h_i = \int_{T_{\mathrm{ref}}}^{T} c_{\mathrm{p}i}\, dT + h^{\circ}{}_{\mathrm{f}i} \tag{4}$$

Standard notations in thermodynamics and fluid mechanics are used in Eqs. (1–4). The mass diffusion velocity V_i consists of contributions from both concentration (i.e., Fick's law) and temperature (i.e., Soret effect) gradients:

$$V_i = -D_i \frac{1}{X_i}\frac{\partial X_i}{\partial x} + D_i \frac{D_{T_i}}{X_i}\frac{1}{T}\frac{\partial T}{\partial x} + V_{\mathrm{cor}} \tag{5}$$

where the correction velocity V_{cor} is employed to ensure that:

$$\sum_{i=t}^{N} Y_i V_i = 0 \tag{6}$$

The ideal gas law for a multicomponent system is derived to close the formulation.

$$p = \rho R_{\mathrm{u}} T \sum_{i=1}^{N} \frac{Y_i}{W_i} \tag{7}$$

Gas-Phase Chemical Kinetics

For a set of N_R elementary reactions involving N species, the reaction equations can be written in the following general form:

$$\sum_{i=1}^{N} \nu'_{ij} M_i \underset{k_{\mathrm{bw}_j}}{\overset{k_{\mathrm{fw}_j}}{\Leftrightarrow}} \sum_{i=1}^{N} \nu''_{ij} M_i, \quad j = 1, 2, \ldots, N_R \tag{8}$$

where V'_{ij} and V''_{ij} are the stoichiometric coefficients for the ith species appearing as a reactant in the jth forward and backward reactions, respectively, and M_i is the chemical symbol for the ith species. The reaction-rate constant k_j (either k_{fw_j} or k_{bw_j}) is given empirically by the Arrhenius expression:

$$k_j = A_j \, T^{B_j} \exp\left(-E_j/R_{\mathrm{u}} \, T\right) \tag{9}$$

The rate of change in molar concentration of the ith species by the jth reaction is:

$$\dot{C}_{ij} = (\nu'_{ij} - \nu''_{ij}) \left(k_{\mathrm{fw}_j} \prod_{i=1}^{N} C_i^{\nu'_{ij}} - k_{\mathrm{bw}_j} \prod_{t=1}^{N} C_i^{\nu''_{ij}}\right) \tag{10}$$

The net rate of mass production of the ith species $\dot{w}_i$ in Eq. (2) is then obtained by summing up the changes due to all reactions:

$$\dot{w}_i = W_i \sum_{j=1}^{N_{\mathrm{R}}} \dot{C}_{ij} \tag{11}$$

It must be noted that the expression for chemical reaction rates, Eq. (10), is valid strictly for elementary reactions. If a global kinetics scheme is used, the exponents for molar concentrations may differ from their stoichiometric coefficients in order to match experimental data.

The detailed reaction mechanism proposed by Yetter [28] and augmented by Lin and co-workers [35] is employed to treat the gas-phase chemistry kinetics. The model was first developed based on a hierarchical approach for collecting kinetic data and the specific chemical sub-models that are required to form the gas-phase combustion mechanism [28]. In particular, three kinetic sub-models of increasing complexity (N_2O decomposition, H_2/NO_2 reaction, and CH_4/N_2O reaction) are established by using the results from kinetics experiments over a broad range of temperature and pressure. When the initial decomposition steps of RDX proposed by Melius [27] are adopted, the overall scheme contains 38 species and 178 reactions. Here, the N–N bond cleavage is assumed to be the first step in the gas-phase decomposition process of RDX due to its weak bond energy of ~50 kcal/mol compared to ~60 kcal/mol for the C–N bond and ~90 kcal/mol for the C–H bond. Li and Williams [36], however, indicated that the initial dominant decomposition pathway might be concerted symmetric triple fission to produce three H_2CNNO_2 fragments at high temperatures. At present, uncertainties still exist about the types of species formed and their associated rates, especially for regions in close proximity to the burning surface. More experimental investigation is needed to clarify the initial decomposition steps of RDX. In the past, the detailed reaction model [28] has been implemented to simulate self-sustained and laser-induced combustion of RDX under steady-state conditions [29]. Reasonably good agreement was obtained with experimental data in terms of propellant burning rate and flame structure. Three deficiencies, however, were observed: 1) insufficient quantities of N_2 and NO_2 in the first stage of flame; 2) abundance of CH_2O at the end of the first stage; and 3) overprediction of the ignition delay. Modifications were thus undertaken to circumvent these problems in three steps. First, a reaction allowing for the formation of N_2 during the initial stage of reaction was added to the model. Second, the rate of thermal decomposition of H_2CN was increased to allow for greater H-radical generation and subsequently for faster consumption of CH_2O. Third, a reaction between H_2CNNO_2 and NO_2 was added to enhance the ignition process. Recently, Lin and coworkers [35] revised the near-surface combustion mechanism by adding more reactions involved in the consumption of H_2CNNO_2, H_2CNNO, H_2CNO, H_2CNOH, and H_2CN. The kinetic rates of these added reactions were determined by using high-level ab initio molecular orbital (MO) and statistical theory calculations [35]. The resulting kinetics scheme, containing 49 species and 250 reactions, can be found in [34].

Subsurface Two-Phase Processes

The liquid and gas bubbles underneath the propellant surface are treated together and referred to as the subsurface two-phase region. The physiochemical processes in this region are extremely complicated, involving an array of intricacies such as thermal decomposition, evaporation, bubble formation, gas-phase reactions in bubbles, interfacial transport of mass and energy between gas and condensed phases, etc. Taking full account of these processes is hardly practical, and many simplifications have been made to render the analysis manageable. A two-phase fluid dynamic model using a spatial averaging technique is employed to formulate the complicated phenomena in the two-phase region [29, 30]. The mass diffusion velocities in the two-phase region V_{gi} and V_{ci} are assumed to be relatively small compared to their convective counterparts in the gas phase, and are ignored to simplify numerical calculations. The conservation equations for both the liquid phase and gas bubbles can be combined into the following form:

Mass

$$\frac{\partial\,[(1-\phi)\,\rho_l + \phi\rho_g]}{\partial t} + \frac{\partial\,[(1-\phi)\,\rho_l u_l + \phi\rho_g\,u_g]}{\partial x} = 0 \qquad (12)$$

Species concentration for liquid phase

$$\frac{\partial[(1-\phi)\,\rho_l\,Y_{li}]}{\partial t} + \frac{\partial}{\partial x}[(1-\phi)\,\rho_l\,u_l\,Y_{li}] = \dot{w}_{li}\ (i = 1,2,\ldots,N_l) \qquad (13)$$

Species concentration for gas phase

$$\frac{\partial\,(\phi\rho_g Y_{gi})}{\partial t} + \frac{\partial(\phi\rho_g\,u_g\,Y_{gi})}{\partial x} = \dot{w}_{gi} \quad (i = 1,2,\ldots,N_g) \qquad (14)$$

Energy

$$\rho_t c_{p,t}\frac{\partial T_t}{\partial t} + \rho_t\,u_t\,c_{p,t}\frac{\partial T_t}{\partial x} = \frac{\partial}{\partial x}\left(\lambda_t\frac{\partial T_t}{\partial x}\right) - \sum_{j=1}^{N_l} h_{lj}\dot{w}_{lj} - \sum_{j=1}^{N_g} h_{gj}\,\dot{w}_{gj} + \sum_{j=1}^{N_g} h_{gj}\,Y_{gj}\dot{w}_{l\to g} - \sum_{j=1}^{N_c} \mathrm{h}_{lj}\,Y_{lj}\dot{w}_{l\to g} + \dot{Q}'''_{rad,l} \qquad (15)$$

where subscript t denotes the mass-averaged quantity in the two-phase region. The source terms, $\dot{w}_{li}$ and $\dot{w}_{gi}$, represent the mass production rates of the ith species in the liquid phase and gas bubbles, respectively, and $\dot{w}_{l\to g}$ represents the mass conversion rate from liquid to gas.

Subsurface Chemical Kinetics and Phase Transition

The global decomposition model of RDX proposed by Brill et al. [37], derived from a well-calibrated temperature-jump/Fourier transform infrared (T-jump/FTIR) spectroscopy experiment, is adopted here. This mechanism includes two pathways as follows:

$$\mathrm{RDX_{(l)}} \xrightarrow{k_1} \mathrm{3CH_2O + 3N_2O} \qquad (R1)$$

$$\mathrm{RDX_{(l)}} \xrightarrow{k_2} \mathrm{3HCN + 3HONO}$$

$$\xrightarrow{\text{fast}} \mathrm{3HCN} + \frac{3}{2}\mathrm{NO} + \frac{3}{2}\mathrm{NO_2} + \frac{3}{2}\mathrm{H_2O} \qquad (R2)$$

Reaction (R1) is an exothermic, low-temperature pathway, whereas Reaction (R2) is an endothermic, high-temperature pathway. The reaction rates are obtained from a model of the T-jump/FTIR experiment [38], which takes into account the heat transfer of the filament and sample.

$$k_1 = 6.00 \times 10^{13} \exp\left(-\frac{36.0\ \mathrm{kcal/mol}}{R_u T}\right) s^{-1} \tag{16}$$

$$\dot{w}_{R1} = (1-\phi)\rho_l k_1$$

$$k_2 = 1.60 \times 10^{17} \exp\left(-\frac{45.0\ \mathrm{kcal/mol}}{R_u T}\right) \mathrm{s}^{-1}$$

$$\dot{w}_{R2} = (1-\phi)\rho_l k_2 \tag{17}$$

The two global decomposition reactions are nearly thermally neutral at temperatures ~600 K. Subsequent reactions among the products of Reactions (R1) and (R2) may occur and provide the energy to sustain pyrolysis. Brill [39] examined several plausible secondary reactions, such as $CH_2O + NO_2$, $CH_2O + N_2O$, and $HCN + NO_2$, and their corresponding reaction rates. Results indicated that the following reaction:

$$NO_2 + CH_2O \xrightarrow{k_3} NO + CO + H_2O \tag{R3}$$

is probably the most important secondary reaction in the subsurface region. The reaction rate of (R3) has been determined from shock-tube experiments [40] and is given by:

$$k_3 = 8.02 \times 10^2\, T^{2.77} \exp\left(-\frac{13.7\ \mathrm{kcal/mol}}{R_u T}\right) \frac{\mathrm{cm}^3}{\mathrm{mol} \times \mathrm{s}} \tag{18}$$

$$\dot{\omega}_{R3} = \phi k_3 \frac{\rho_g Y_{CH_2O}}{W_{CH_2O}} \frac{\rho_g Y_{NO_2}}{W_{NO_2}}$$

In addition to the thermal decomposition and its subsequent reactions (R1–R3), thermodynamic phase transition from liquid to vapor RDX is considered to provide a complete description of the mass conversion process.

$$RDX_{(l)} \Leftrightarrow RDX_{(g)} \tag{R4}$$

Based on gas kinetic theory, the net evaporation rate is taken to be the difference between the evaporation and condensation rates [29, 30] and is expressed as:

$$\dot{m}''_{\mathrm{net}} = \mathrm{s}\left(\frac{1}{4}\sqrt{\frac{8R_u T}{\pi W_{\mathrm{RDX}}}}\right)\frac{pW_{\mathrm{RDX}}}{R_u T}\left(\frac{p_{\mathrm{v\cdot eq}}}{p} - X_{\mathrm{RDX}}\right) \tag{19}$$

Thus, the specific mass conversion rate due to evaporation becomes:

$$\dot{w}_{R4} = A_{\mathrm{sp}}\dot{m}''_{\mathrm{net}} \tag{20}$$

The specific surface area A_{sp} is a function of void fraction and number density of bubbles, and is derived as follows:

$$A_{\mathrm{sp}} = (36\pi n)^{1/3}\phi^{2/3}, \quad \phi < 1/2$$
$$\text{or } (36\pi n)^{1/3}(1-\phi)^{2/3}, \ \phi > 1/2 \tag{21}$$

where n is the number density of gas bubbles to be determined empirically [30].

Solid-Phase Processes

Because very little RDX decomposes in the solid phase due to its low-temperature conditions, only the energy conservation equation that includes both conductive and radiative heat transfer is required to model the solid-phase processes. The equation takes the form:

$$\rho_s c_{p,s}\frac{\partial T_s}{\partial t} + \rho_s u_s c_{p,s}\frac{\partial T_s}{\partial x} = \frac{\partial}{\partial x}\left(\lambda_s \frac{\partial T_s}{\partial x}\right) + \dot{Q}'''_{\mathrm{rad,s}} \tag{22}$$

where subscript s represents solid. The thermal properties of RDX were recently measured by Hanson–Parr and Parr [41]. Because the properties of liquid RDX, such as λ_l and $c_{p\cdot l}$, are not available in the literature, the same values are used for both the liquid and solid RDX. Table 2 lists the thermodynamic and transport properties of RDX used in the current work.

Radiative Heat Transfer

The radiative heat-transfer processes are complicated and difficult to model, usually including absorption, emission, and scattering of radiant energy in both the gas and condensed phases, as well as surface absorption, transmission, and reflection. In this work, the focus is on a CO_2

TABLE 2

Thermophysical Properties of RDX

Parameter	Units	Value	Ref.
$c_{p,s}$	cal/gK	$4.861 \times 10^{-3} + 0.843 \times 10^{-3} \times T$	[41]
$c_{p,l}$	cal/gK	$4.861 \times 10^{-3} + 0.843 \times 10^{-3} \times T$	[41]
λ_s	cal/K s cm	0.665×10^{-3}	[41]
λ_l	cal/K s cm	0.665×10^{-3}	[41]
H_v	kcal/mol	26.8	[32]
H_{fus}	kcal/mol	8.1	[42]
H_{sub}	kcal/mol	34.9	$H_v + H_{fus}$
ρ_s	g/cm^3	1.8	[42]
ρ_l	g/cm^3	1.8	[42]
T_m	K	478	[42]

laser with a wavelength of 10.6 μm. The following assumptions are made to render the analysis feasible. First, the CO_2 laser is treated as collimated irradiation and locally one-dimensional. Second, reflection at the propellant surface is not considered because the normal reflectivity of RDX with a refractive index of 1.49 at 10.6 μm was estimated to be only 0.047, using Fresnel's equation [43]. Third, the levels of scattering by and emission from the gas-phase, two-phase, and solid-phase regions are assumed to be relatively small compared to that of absorption. Finally, Beer's law is employed to determine the volumetric absorption in the solid- and two-phase regions as follows.

Absorption in Solid and Subsurface Two-Phase Regions ($x < 0$)

$$\dot{Q}'''_{\text{rad,c}} = (1 - f_g - \alpha_{\text{sur}})\,(1 - \phi)\,\beta_c\, e^{(1-\phi)\,\beta_c x}\, \dot{Q}''_{\text{laser}} \quad (c = \text{liquid, solid}) \tag{23}$$

where f_g is the fraction of laser energy absorbed in the gas-phase region, α_{sur} the fraction of laser heat flux absorbed by the propellant surface, β_c the absorption coefficient, and $\dot{Q}''_{\text{laser}}$ the laser heat flux. The absorption coefficient of solid RDX for a CO_2 laser at a wavelength of 10.6 μm has been measured by Isbell and Brewster [43] to be 2800/cm. Because the absorption properties of many types of semi-transparent liquids are quite similar to those of solids [44], the absorption coefficients of solid and liquid RDX are assumed to be the same in this work. The fraction of laser energy absorbed in the gas-phase region f_g is defined by the following equation:

$$f_g = \frac{\int_0^\infty \dot{Q}'''_{\text{rad,g}}\, dx}{\dot{Q}''_{\text{laser}}} \tag{24}$$

where $Q'''_{\text{rad,g}}$ is the gas-phase absorption of laser energy, and can be estimated by examining the infrared transmittance data. Figure 2a shows the spectrum for vapor RDX and its gaseous decomposition products, obtained by rapidly heating a 2-mg sample of RDX using confined rapid thermolysis FTIR spectroscopy [45]. A detailed description of the experiments is available in [45]. Strong, broad absorption bands of vapor RDX are present in a wavelength range of 4.7 to 13.3 μm. The same absorption bands were also observed by Brill from rapid-scanning FTIR spectroscopy [46]. The absorption characteristics of the gaseous decomposition products of RDX at 10.6 μm can be readily studied from their corresponding individual IR spectra [47]. None of the major decomposition products exhibits a noticeable absorption at 10.6 μm. It is clearly evident that of the species present only vapor RDX absorbs a considerable amount of CO_2 laser energy in the gas phase. Thus, volumetric absorption in the gas phase is given by:

$$\dot{Q}'''_{\text{rad,g}} = C_{\text{RDX}} A_\nu \kappa_{\text{RDX,g}} \dot{Q}''_{\text{laser}} \tag{25}$$

where C_{RDX} is the molar concentration of vapor RDX, and A_ν is Avogadro's constant. The ab-

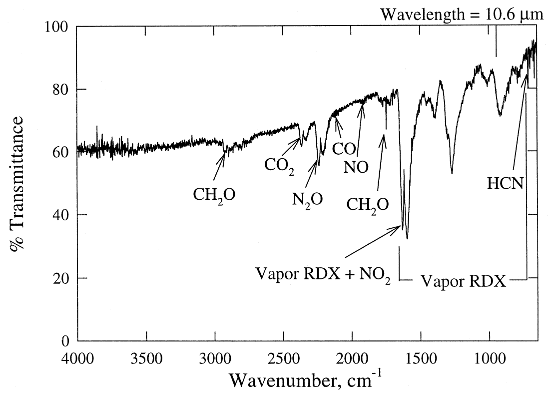

(a) Vapor RDX and its gaseous decomposition products.

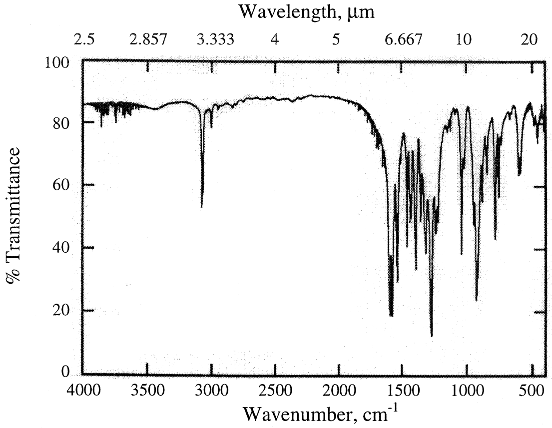

(b) Solid RDX.

Fig. 2. Infrared transmittance spectra for (a) vapor RDX and its gaseous decomposition products [45] and (b) solid RDX [48].

sorption cross-section of vapor RDX, $\kappa_{\mathrm{RDX,g}}$, is defined as:

$$\kappa_{\mathrm{RDX,g}} = \frac{\beta_c W_{\mathrm{RDX}}}{\rho_{\mathrm{RDX,c}} A_v} \tag{26}$$

Because the absorption properties of vapor RDX are not available in the literature, the absorption coefficient β_c is used to estimate $\kappa_{\mathrm{RDX,g}}$ with the assumption that the characteristics of vibration-rotational bands of vapor RDX at the wavelength of interest are similar to those of intermolecular vibration bands of condensed RDX [44]. Figure 2b shows the IR transmittance spectrum for solid RDX, obtained from the measurement of RDX powder pressed in a KBr matrix [48]. Similar to the absorption characteristics of vapor RDX, a strong absorption band of solid RDX at 10.6 μm is clearly evident. At present, the use of the same absorption properties for both condensed and vapor RDX seems to be reasonable, due to the lack of measured data. Note that a parametric study has also been performed by varying the absorption coefficient of vapor RDX by 20% in order investigate the effect of absorption properties on the overall ignition process.

Boundary Conditions

The physical processes in the gas-phase and subsurface regions must be matched at the interface by requiring continuities of mass and energy fluxes. This procedure eventually determines propellant surface conditions and burning rate as the eigenvalues of the problem. The interfacial boundary conditions are expressed as follows:

Mass

$$(\rho u)_{0^+} = [(1-\phi)\rho_l u_l + \phi \rho_g u_g]_{0^-} \tag{27}$$

Species concentration

$$[\rho(u+V_i)Y_i]_{0^+} = [(1-\phi)\rho_l u_l Y_{li} + \phi \rho_g u_g Y_{gi}]_{0^-} \tag{28}$$

Energy

$$\left[\lambda \frac{dT}{dx}\right]_{0^+} + \alpha_{\mathrm{sur}} \dot{Q}''_{\mathrm{laser}} = \left[\lambda_t \frac{\mathbf{dT}}{\mathbf{dx}}\right]_{\mathbf{0}^-} + (1-\phi)\rho_l u_l \frac{H_v}{W_{\mathrm{RDX}}} \tag{29}$$

where subscripts 0^+ and 0^- represent conditions at the interface on the gas phase and subsurface sides, respectively. Note that Eq. (27) is essentially the summation of mass fluxes of all species governed by Eq. (28), and thus can not be independently used for determining the eigenvalues. An additional condition is required. Here, the thermodynamic phase transition from liquid to vapor RDX is assumed to prevail at the interface, giving:

$$(\rho_l u_l)_{0^-} = \dot{m}''_{\mathrm{net}} \tag{30}$$

Equations (28–30), coupled with the assumptions that $T_g = T_l$ and $\rho_g u_g = \rho_l u_l$ in the condensed phase, are sufficient to solve the set of unknowns (u_l, T, ϕ, Y_i) at the propellant surface.

The far-field conditions for the gas phase require the gradients of flow properties to be zero at $x \rightarrow \infty$.

$$\frac{\partial \rho}{\partial x} = \frac{\partial u}{\partial x} = \frac{\partial Y_i}{\partial x} = \frac{\partial T}{\partial x} = 0 \text{ at } x \rightarrow \infty \tag{31}$$

The condition at the cold boundary for the solid phase ($x \rightarrow -\infty$) is

$$T_s = T_{\text{ini}} \text{ at } x \rightarrow -\infty \tag{32}$$

Finally, the conditions for the phase transition from solid to liquid at the melting point (T_m = 478 K) are required.

$$T_s = T_t = T_m \quad \text{and} \qquad \text{at } x = x_m \tag{33}$$

$$k_t \left.\frac{\partial T_t}{\partial x}\right|_{x_{m^+}} = k_s \left.\frac{\partial T_s}{\partial x}\right|_{x_{m^-}} - \frac{\rho_s H_{\text{fus}}}{W_{\text{RDX}}} \left(\frac{dx_m}{dt} - u_{1,0^-} \right)$$

where subscripts x_m^+ and x_m^- represent conditions at the interface on the two-phase and solid-phase sides, respectively.

NUMERICAL METHOD

The theoretical formulation established in the preceding section requires a time-accurate analysis. A dual-time-stepping numerical integration method is employed to circumvent the computational difficulties associated with the rapid transients during the ignition process [30, 34]. The scheme includes artificial time derivatives, so that the solution converged in pseudo-time corresponds to a time-accurate solution in physical time. The physical time step is chosen to be ~1/100 of the estimated ignition delay, or even less, to obtain reasonable temporal resolution. When marching from one physical time level to the next, all the conservation equations and associated boundary conditions are solved by treating the propellant surface temperature T_{sur} and burning rate r_b as the eigenvalues. The iteration starts with guessed T_{sur} and r_b, which are bounded by Eq. (30). The condensed- and gas-phase governing equations are solved with these guessed values and other boundary conditions. If the resulting temperature gradients do not satisfy the interfacial energy balance equation, Eq. (29) is used to correct the values of T_{sur} and r_b by means of a bisection method. The updated T_{sur} and r_b are then substituted into the governing equations for another solution of the temperature field. The iterative procedures are performed until T_{sur} and r_b converge, and Eq. (29) is satisfied. Finally, a solution at the physical time level is obtained when all the governing equations and associated boundary conditions are satisfied. In general, the gas-phase solver takes much more computational time than its counterpart for the condensed phase, due to the complexity of the chemical kinetics in the gas phase.

Calculations of chemically reacting flows often encounter numerical stiffness problems attributed to the wide variety of time and length scales associated with chemical reactions and transport processes. The problem can be effectively circumvented by using a combined Newton iteration and (pseudo-) time-integration scheme originally developed by Kee et al. [49]. The Newton method works efficiently for linear systems but may fail to converge for nonlinear systems unless a reasonable initial guess is provided. Conversely, the (pseudo-) time-integration technique is more robust, but less efficient. To optimize the benefits of these two algorithms, computations usually start with the Newton method, and then switch to the time-integration scheme when the iteration fails to converge. After another trial solution is obtained with several time-marching steps, the Newton method is resumed to gain efficiency. The time step in the time-integration technique is sufficiently smaller than the physical time step in order to handle the numerical problems caused by the highly transient phenomena due to rapid chemical reactions. An adaptive grid system is employed to further improve the convergence rate.

A four-step Runge–Kutta method is used for temporal integration of the condensed-phase conservation equations, along with a second-order central differencing scheme for spatial discretization. Calculations start with an estimate of the temperature profile obtained by solving an inert energy equation. The conservation equations of mass and species concentra-

TABLE 3

Ignition Delay of Gaseous RDX in Well-Stirred Reactor at 1 atm (Unit: ms)

Initial species concentrations*	500 K	600 K	700 K	800 K	900 K
100% RDX	>1000	36.2	2.37	1.20	0.605
0.9 RDX + 0.1Ar	>1000	36.6	2.57	1.30	0.648
0.9 RDX + others**	>1000	80.7	2.05	1.08	0.552
0.515 RDX + others***	>1000	169	1.85	0.773	0.408

* By mole.

** $0.025(CH_2O + N_2O) + 0.01(2HCN + NO_2 + NO + H_2O)$.

*** $0.08(CH_2O + N_2O) + 0.065(2HCN + NO_2 + NO + H_2O)$.

tion are then integrated with the given temperature profile. The energy equation is subsequently solved with the newly obtained void fraction and species concentration profiles to update the temperature profile. Because these equations are solved sequentially, iteration is required to get a converged solution. Once the temperature reaches the melting temperature, the movement of the solid–liquid interface is determined from Eq. (31). The fixed-grid Eulerian method [34, 50] is employed for interface tracking.

DISCUSSION OF RESULTS

Ignition of Gaseous RDX

The ignition characteristics of gaseous RDX were first studied by using the SENKIN program [51], which performs integration of the mass and energy conservation equations for a homogeneous mixture in an adiabatic, constant-pressure environment. The purposes of this analysis were to identify the heat-release mechanisms for achieving ignition and to examine the dependence of ignition delay on initial temperature and species concentrations. The chemical kinetics scheme involves 49 species and 250 elementary reactions, as discussed earlier [34]. Table 3 lists the predicted result of ignition delay, defined as the time required for the temperature to reach 2500 K. This condition also corresponds to the formation of CN species, which gives rise to a luminous flame and often serves as an ignition criterion for both experimental and theoretical studies. For all the cases studied here, ignition occurs only if the initial temperature exceeds 600 K. Figures 3 and 4 present the temporal evolution of temperature and species concentration, respectively, for T_{ini} = 700 K and 100% RDX. Results of other cases show a similar trend, but the events become shorter with increasing initial temperature. The overall gaseous RDX ignition process can be divided into five distinct stages: thermal decomposition, first oxidation, chemical preparation, second oxidation, and completion stages. In Stage I, RDX decomposes to low-molecular weight species, such as CH_2O, N_2O, NO_2, HCN, and HONO. This decomposition process is slightly endo-/exo-thermic or thermally neutral depending on the initial temperature. In Stage II, oxidation reactions occur and release a significant amount of energy with the temperature reaching ~1500 K. The dominant net reactions in Stage II can be given as follows.

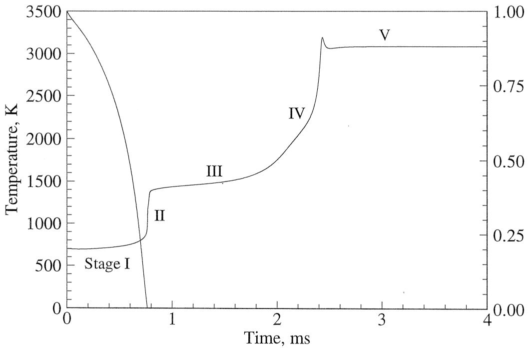

Fig. 3. Temporal evolution of temperature and RDX concentration during ignition in well-stirred reactor.

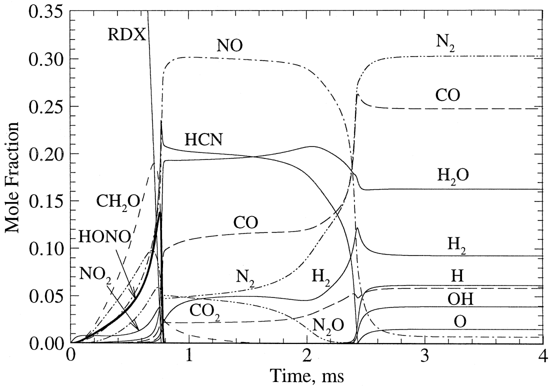

Fig. 4. Temporal evolution of species concentrations during RDX ignition in well-stirred reactor.

$$CH_2O + NO_2 \Rightarrow H_2O + NO + CO \qquad (-44\ \text{kcal/mol}) \quad (R5)$$

$$HNO + HONO \Rightarrow H_2O + 2NO \qquad (-23\ \text{kcal/mol}) \quad (R6)$$

$$2HCN + NO_2 \Rightarrow C_2N_2 + NO + H_2O \qquad (-33\ \text{kcal/mol}) \quad (R7)$$

$$CO + NO_2 \Rightarrow CO_2 + NO \qquad (-53\ \text{kcal/mol}) \quad (R8)$$

$$2HONO \Rightarrow NO + NO_2 + H_2O \qquad (8\ \text{kcal/mol}) \quad (R9)$$

$$2NO_2 \Rightarrow 2NO + O_2 \qquad (29\ \text{kcal/mol}) \quad (R10)$$

The heat release in Stage II is mainly caused by the conversion of CH_2O and NO_2 to H_2O, NO, and CO, and to a lesser extent by the reactions of HCN and HONO. Stage III represents the chemical preparation time before the second oxidation reactions (Stage IV) take place. The species formed in Stage II are relatively stable, due to the high activation energies of their associated reactions, and require a finite time to oxidize further. The highly exothermic reactions occurring in Stage IV may be attributed to the following net reactions.

$$2HCN + 2NO \Rightarrow 2CO + 2N_2 + H_2 \qquad (-158\ \text{kcal/mol}) \quad (R11)$$

$$N_2O + H_2 \Rightarrow N_2 + H_2O \qquad (-78\ \text{kcal/mol}) \quad (R12)$$

$$C_2N_2 + 2NO \Rightarrow 2CO + 2N_2 \qquad (-169\ \text{kcal/mol}) \quad (R13)$$

Figure 4 indicates that the reduction of HCN and NO to N_2, CO, H_2O, and H_2 is largely responsible for the heat release in Stage IV. Finally, all the final products are formed; no further reactions occur in Stage V.

If RDX does indeed decompose in the condensed phase during the laser-induced ignition process, the decomposition products at the propellant surface may affect the gas-phase chemistry. In order to account for the various possible surface conditions, the effect of initial species concentration on the heat-release mechanism was also investigated, giving the results shown in Table 3. Over the initial temperature range studied, the addition of argon prolongs ignition through its adverse influence on heat release during the initial stage. When some of the RDX decomposition products, such as CH_2O, N_2O, HCN, NO_2, NO, and H_2O, are initially mixed with gaseous RDX in the system, the ignition delays for $T_{\text{ini}} \geq 700$ K are considerably reduced due to the exothermic reactions involved with these additional decomposition products at high temperatures (≥700 K). However, for $T_{\text{ini}} = 600$ K, the ignition delay increases with increasing initial concentrations of the decomposition products and becomes much longer than that of RDX/Ar (Table 3). This result indicates that the reactions involved with the added decomposition products do not take place at low temperatures (≤600 K). Thus, the heat release, in the low temperature range, can only be attributed to thermal decomposition of RDX. As shown in Table 3, the ignition delay becomes longer for both 90 mol.% and 51.5 mol.% RDX mixed with the decomposition products, compared to the system initially containing 90 mol.% RDX and 10 mol.% Ar, because a smaller amount of RDX is initially available for RDX decomposition.

Laser-Induced Ignition of RDX

The entire laser-induced ignition process of RDX in an argon environment has been studied in detail. Figure 5 shows the predicted temporal evolution of the temperature field at an incident laser heat flux of 400 W/cm^2 under atmospheric pressure. The initial temperature is 300 K. The interface between the subsurface and gas-phase regions is set to be $x = 0$, with negative and positive values of the x-coordinate representing the subsurface and gas phase, respectively. The surface temperature is rapidly increased to 475

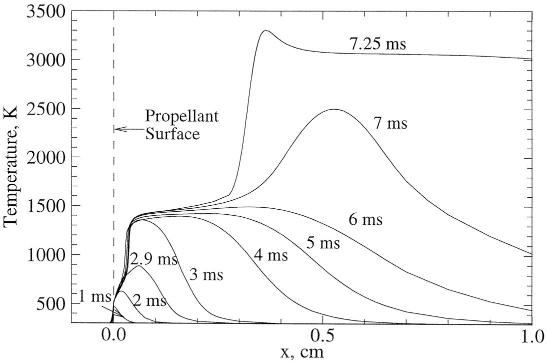

Fig. 5. Evolution of temperature field during laser-induced ignition of RDX in argon at $p = 1$ atm and $\dot{Q}''_{\mathrm{laser}} = 400$ W/cm^2.

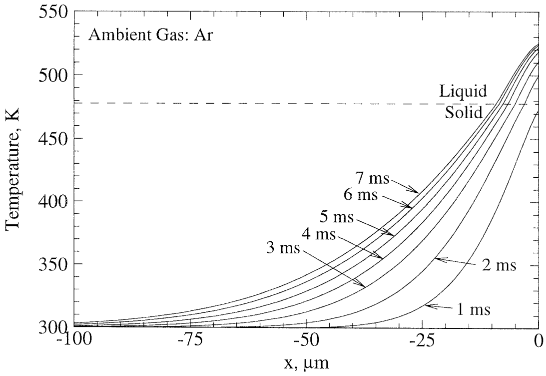

Fig. 6. Close-up view of temperature evolution in subsurface region during laser-induced ignition of RDX at $p = 1$ atm and $\dot{Q}''_{\mathrm{laser}} = 400$ W/cm^2.

K within 1 ms, due to the high intensity of laser heat flux. The profiles for $t < 1$ ms represent inert heating of the thin surface layer with conductive heat losses to both the solid- and gas-phase regions. The temperature rises in the gas phase at $t = 2$ ms are primarily caused by radiant energy absorption rather than exothermic reactions, because the extent of RDX decomposition in the gas phase is very limited at this stage of the event. At $t = 2.9$ ms, exothermic gas-phase reactions start to occur, and a flame appears near the propellant surface at $t = 3$ ms. During the time period between 3 and 6 ms, the temperature continues to increase to ~1500 K, as a consequence of the heat release by exothermic reactions. As time further elapses, a luminous flame appears, and the temperature rises to its adiabatic temperature. The luminous flame is not stationary but regresses toward the surface. It is worth noting that a dark-zone temperature plateau (at $T \sim 1500$ K) is formed in the laser-assisted combustion of RDX, while the existence of the dark zone was not evident in the self-assisted combustion [29]. There is a time lag (~4 ms) between the first appearances of the primary and secondary flames.

Figure 6 shows a close-up view of the temperature evolution in the condensed phase near the propellant surface. The transient development of thermal wave penetration into the subsurface region is clearly observed. The characteristic thickness of the thermal layer in the subsurface region is much thinner than that in the gas-phase region. Phase transition from solid to liquid can be indicated by the distinct change of temperature gradient at $T_m = 478$ K. Because most of the CO_2 laser heat flux is absorbed by the thin surface layer due to the high absorption coefficient (2800/cm) of RDX at the wavelength of 10.6 μm, the formation of the mushy zone can be safely ignored in the current work. However, some propellants, including RDX, are quite transparent to plasma irradiation in the ultraviolet/visible wavelength range; thus, the appearance of the mushy zone may be evident in that situation. Figure 7 shows the distributions of void fraction and species concentrations in the subsurface two-phase region when ignition is achieved at $t = 7$ ms. The extent of RDX decomposition in the condensed phase is very limited during the laser-induced ignition process, due to the short residence time and low-temperature conditions.

Figures 8 to 13 show the temperature and species-concentration fields in the gas phase at

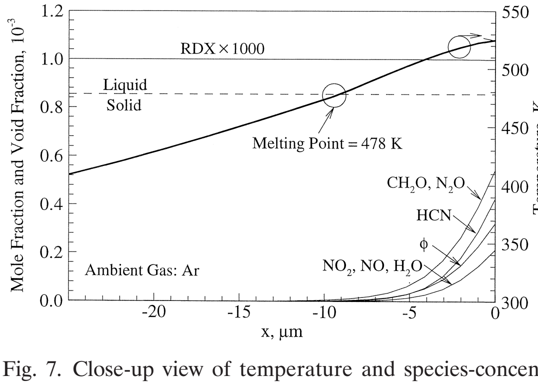

Fig. 7. Close-up view of temperature and species-concentration profiles in subsurface region at $t = 7$ ms ($p = 1$ atm and $\dot{Q}''_{\mathrm{laser}} = 400$ W/cm^2).

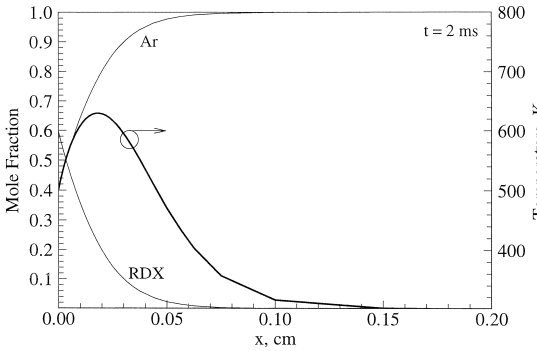

Fig. 8. Temperature and species-concentration profiles in gas phase at $t = 2$ ms.

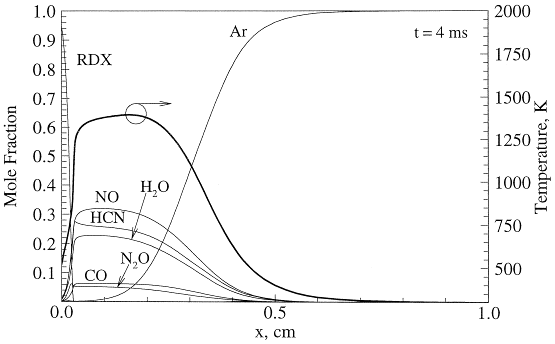

Fig. 10. Temperature and species-concentration profiles in gas phase at $t = 4$ ms.

various times. At $t = 2$ ms, the gas temperature increases by more than 300 K, although only a small fraction (less than 10%) of the laser energy is absorbed in the gas phase. This is not surprising, because the heat capacity of the gas mixture is much lower than that of the condensed mixture. At $t = 2.9$ ms, small amounts of intermediate species, such as HCN, NO, HONO, CH_2O, N_2O, and NO_2, result from thermal decomposition of RDX. The temperature rises to more than 800 K within 1 mm above the surface. Figure 10 shows the first appearance of the primary flame at $t = 4$ ms. The aforementioned RDX decomposition products, especially CH_2O and NO_2, undergo rapid reactions, which leads to the formation of NO, HCN, H_2O, CO, and N_2O in the flame. The dominant net reactions in the primary flame zone can be given by (R5–R10). The temperature increases to ~1400 K. The species formed in the primary flame are relatively stable due to the high activation energies of their associated reactions, and require a finite time to oxidize further. At this stage, the fraction of laser absorption decreases significantly because of the rapid consumption of RDX, which is considered to be the only species absorbing a noticeable amount of laser energy in the gas phase. Figure 11 shows more details of the chemistry involved in the primary flame. The conversion of CH_2O, NO_2, and HONO to NO, CO, HCN, etc. appears to be the major chemical mechanism releasing thermal energy. Figures 12 and 13 show the development of the secondary flame at $t = 7$ and 7.25 ms, respectively. The temperature increases from 1500 to 3000 K at this stage, and the heat release can be largely attributed to Reactions (R11–R13). The conversion of HCN and NO to the final products seems to be the dominant net reaction in the secondary flame. Once the secondary flame appears, the intense energy release and heat transfer causes the flame to regress toward the propellant surface.

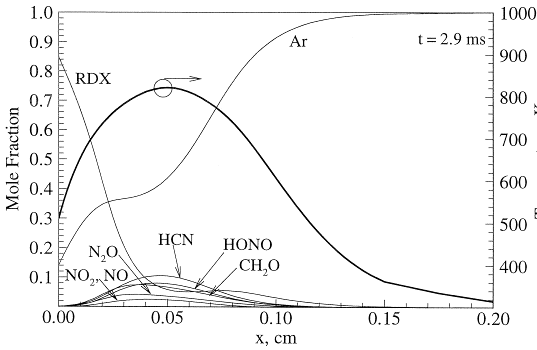

Fig. 9. Temperature and species-concentration profiles in gas phase at $t = 2.9$ ms.

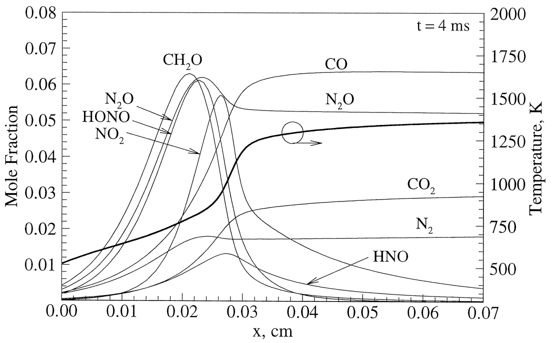

Fig. 11. Close-up view of temperature and species-concentration profiles in primary flame zone at $t = 4$ ms.

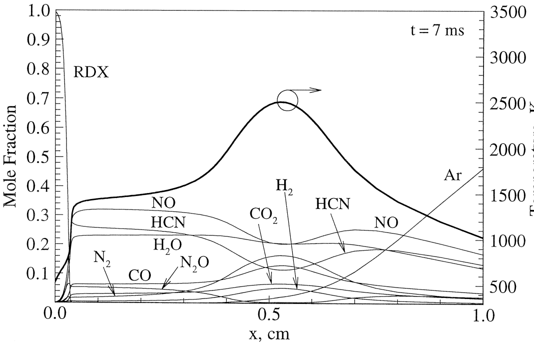

Fig. 12. Temperature and species-concentration profiles in gas phase at $t = 7$ ms.

A parametric study for investigating the effect of the absorption coefficient of vapor RDX on the overall ignition process has been performed by varying the absorption coefficient by 15%. As shown in Fig. 8, the gas-phase temperature is rapidly increased by more than 300 K at $t = 2$ ms, with a small amount of the laser energy absorbed by the gas phase. At $t = 2.9$ ms, the gas-phase temperature rises to more than 800 K, caused by the heat release from the exothermic decomposition reactions in the gas phase. After the inert heating, the heat release from the exothermic reactions becomes much more pronounced than the laser energy absorbed by the gas phase. Because only a small amount of the laser energy was absorbed by the gas phase, a change by 15% in absorption coefficient did not influence the inert heating time significantly. Overall, the effect of the absorption coefficient of vapor RDX on the CO_2 laser-induced ignition was not noticeable over the parameter range studied herein.

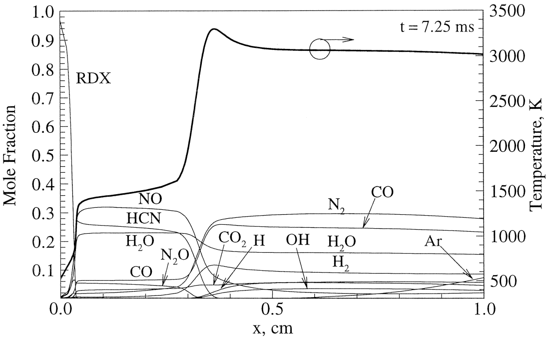

Fig. 13. Temperature and species-concentration profiles in gas phase at $t = 7.25$ ms.

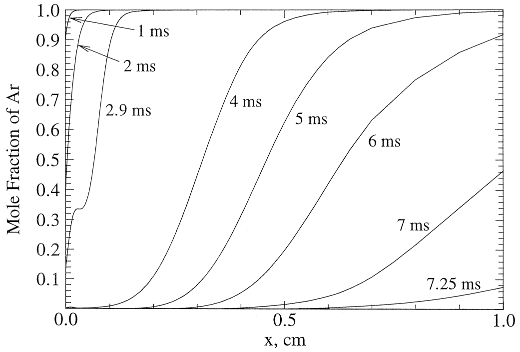

Fig. 14. Concentration profiles of argon at various times.

Figure 14 shows the temporal evolution of the mass fraction of argon, which initially occupies the entire gas-phase region. The argon gas is gradually blown away from the surface by the evolved RDX and gas products. Figure 15 shows the concentration profiles of CH_2O at various times. At 2.9 ms, CH_2O starts to evolve from thermal decomposition of RDX and is rapidly consumed in the primary flame after 4 ms. The trend of evolution of CH_2O is similar to that of N_2O, HONO, NO_2, H_2CN, and H_2CNNO_2. Figure 16 shows the evolution of the NO concentration field. NO is largely formed in the primary flame, and its reduction to N_2 serves as a major heat-release mechanism for raising temperature in the secondary flame. HCN behaves in a similar manner. Figure 17 shows the evolution of the CN concentration field. A noticeable amount of CN is observed at $t > 7$ ms. The concentrations of CN are usually small, except in the secondary flame, thereby serving as a good indication of the flame position. Parr and Hanson– Parr [52] conducted pioneering

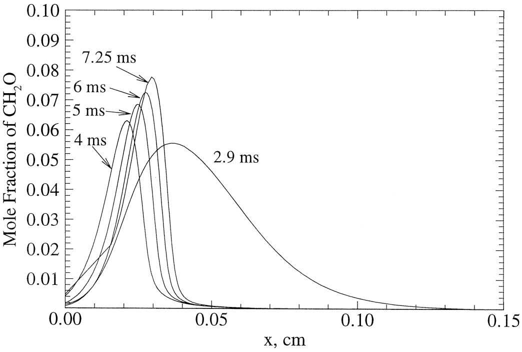

Fig. 15. Concentration profiles of CH_2O at various times.

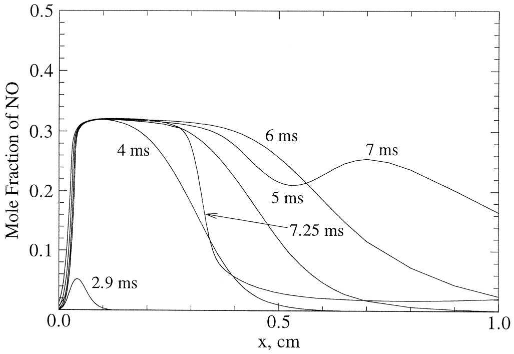

Fig. 16. Concentration profiles of NO at various times.

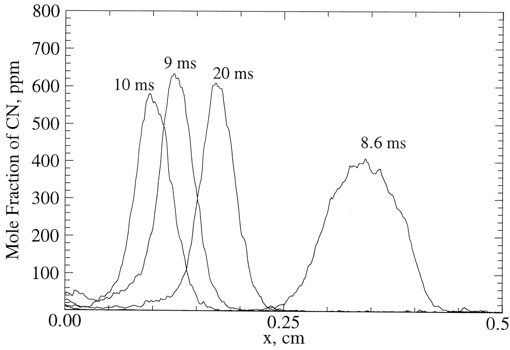

Fig. 18. Measured concentration profiles [52] of CN at various times.

measurements of the transient flame structure of RDX using both ultraviolet-visible absorption and nonintrusive planar laser-induced fluorescence. The experiments were performed at three intensity levels of CO_2 laser heat flux (i.e., 195, 402, and 807 W/cm^2) under atmospheric pressure. Figure 18 shows the measured CN concentration profiles at various times for a laser flux of 402 W/cm^2. Comparison between Figs. 17 and 18 shows good agreement in terms of the CN concentration level. The measured ignition delay time (8.6 ms), however, is slightly longer than the predicted value ($\sim$7 ms), whereas the predicted flame-standoff distance, defined as the location of the peak value of CN concentration profile, is slightly longer than the measurement.

Figure 19 shows the calculated and measured ignition delays of RDX induced by CO_2 laser under atmospheric pressure. Excellent agreement is achieved between the predicted and experimental data for laser intensities less than 200 W/cm^2. For 400 W/cm^2, the predicted ignition delay matches the measurements by Parr et al. [52] and Lee and Litzinger (private communication, Pennsylvania State university, 1995) However, the measured data of Vilyunov and Zarko [4] do not agree with the model prediction for laser intensities above 200 W/cm^2. Vilyunov and Zarko showed that the ignition delay increases with increasing laser intensity above 200 W/cm^2, whereas the results of the current model as well as Parr et al. [52] and Lee and Litzinger (private communication, Pennsylvania State university, 1995) revealed the opposite trend. Vilyunov and Zarko [4] stated that the RDX ignition was controlled by the solid-phase kinetics at low laser intensities (below 200 W/cm^2), whereas the gas-phase kinetics along with the liquid-phase decomposition governed the ignition process at high laser intensities. The current model, however, predicted that the gas-phase chemistry controlled the ignition process

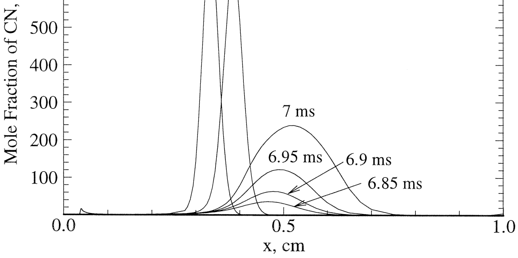

Fig. 17. Predicted concentration profiles of CN at various times.

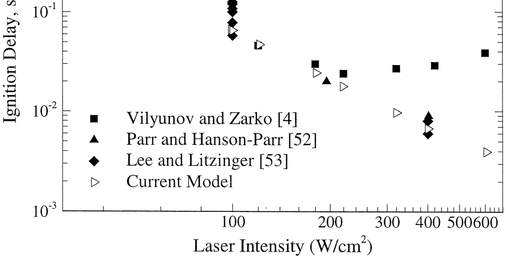

Fig. 19. Effect of CO_2 laser intensity on ignition delay of RDX monopropellant.

over the laser intensity range studied. Thus, the ignition delay became shorter at higher laser intensities, because the gasification rate at the propellant surface increased with increasing laser intensity. Vilyunov and Zarko [4] performed their experiment in both nitrogen and air under atmospheric pressure and found that the ignition delays were about the same within the measurement accuracy. Lee and Litzinger (personal communication pennsylvania State university, 1995) utilized argon as an inert gas, whereas Parr and Hanson–Parr perform the experiment in air. The differences in ignition delay among these three sets of measured data, especially above 200 W/cm^2, can also be attributed to the variation in RDX sample preparation in each experiment. The RDX samples used by Parr and Hanson–Parr [52] and Lee and Litzinger (personal communication Pennsylvania State university, 1995) were pressed military-grade RDX. Information about the samples used by Vilyunov and Zarko [4] was not available.

In the experiment by Parr and Hanson–Parr [52], a significant time lag was obtained between the first light and go/no-go times (~85–100 ms). First light was defined as the time when the luminous flame was first detected, whereas go/no-go was the time when a stable flame was achieved without the laser-assisted heating. The model predictions for the first light and go-no-go times, however, were about the same. In the experiments [52], the luminous flame progressed toward the surface immediately after the first light and moved away from the surface after the maximum temperature gradient was achieved near the surface. The model, however, did not predict this type of flame movement. The luminous flame continuously progressed toward the surface until steady-state deflagration was achieved. The discrepancy between model predictions and experimental observations may be attributed to the heat loss to the ambience. The entire ignition process was treated as adiabatic in the model, whereas heat losses from both the gas-phase flame and the condensed-phase region to the surrounding might be significant in the experiments, in which continuous laser heating was required in order to achieve self-sustained combustion by fully establishing the condensed flame. This suggests that during the ignition stage, heat loss in the condensed phase was too rapid compared to the heat transfer from the gas-phase flame to the surface.

The discrepancies among the existing experimental results may be attributed to the uncertainties associated with measurements under different types of experimental conditions. It is clearly evident that more measured data is needed for model validation. Nonetheless, the present model provides detailed insight into the key physiochemical processes involved in the laser-induced ignition of RDX, and can be effectively used to estimate ignition delay, heat release mechanisms, and flame structure.

CONCLUDING REMARKS

A comprehensive analysis has been performed to investigate the transient ignition behavior of RDX monopropellant over a wide range of CO_2 laser intensity. The model accommodates detailed chemical kinetics and transport phenomena in the gas phase, and thermal decomposition and phase transition in the condensed phase. A chemical kinetics scheme, containing 49 species and 250 reactions, was employed to study the gas-phase flame evolution and related heat-release mechanism. The movement of the solid–liquid interface was determined from an interfacial energy balance. The predicted ignition delay shows good agreement with experimental data. The propellant gasification rate increases with increasing laser intensity, which in turn gives rise to a shorter ignition delay. At present, uncertainties still exist about the thermophysical properties and condensed-phase kinetics of RDX. Nonetheless, the model is capable of treating the entire ignition process from surface pyrolysis to steady-state combustion, with the instantaneous burning rate and surface conditions treated as part of the solution.

This work was sponsored partly by The Pennsylvania State University and partly by the California Institute of Technology Multidisciplinary University Research Initiative under ONR Grant No. N00014-95-1-1338. The authors are indebted to Drs. Tim Parr and YoungJoo Lee for valuable data and helpful discussions.

REFERENCES

1. Price, E. W., Bradley, H. H. Jr., Dehority, G. L., and Ibiricu, M. M., *AIAA J.* 4:1153–1181 (1966).
2. Kulkarni, A. K., Kumar, M., and Kuo, K. K., *AIAA J.* 20:243–244 (1982).
3. Hermance, C. E., in *Fundamentals of Solid Propellant Combustion, Vol. 90* (K. Kuo and M. Summerfield, Eds.) Progress in Astronautics and Aeronautics Series, AIAA, New York, 1984, pp. 239–304.
4. Vilyunov, V. N., and Zarko, V. E., *Ignition of Solids*. Elsevier Science Publishers, New York, 1989.
5. Strakouskiy, L., Cohen, A., Fifer, R., Beyer, R., and Forch, B., *Laser Ignition of Propellants and Explosives*. ARL-TR-1699, Army Research Laboratory, Aberdeen Proving Ground, MD, 1998.
6. Baer, S. D., and Ryan, N. W., *AIAA J.* 6:872–877 (1968).
7. Bradley, H. H., *Combust. Sci. Technol.* 2:11–20 (1970).
8. Linan, A., and Williams, F. A., *Combust. Sci. Technol.* 3:91–98 (1971).
9. Linan, A., and Williams, F. A., *Combust. Flame* 18: 85–97 (1972).
10. Williams, F. A., *AIAA J.* 4:1354–1357 (1966).
11. Waldman, C. H., and Summerfield, M., *AIAA J.* 7:1359–1361 (1969).
12. Waldman, C. H., *Combust. Sci. Technol.* 2:81–93 (1970).
13. Bradley, H. H., and Williams, F. A., *Combust. Sci. Technol.* 2:41–52 (1970).
14. Andersen, W. H., *Combust. Sci. Technol.* 2:23–221 (1970).
15. Andersen, W. H., *Combust. Sci. Technol.* 5:43–46 (1972).
16. Andersen, W. H., *Combust. Sci. Technol.* 5:75–81 (1972).
17. Linan, A., and Crespo, A., *Combust. Sci. Technol.* 6:223–232 (1972).
18. Niioka, T., *Combust. Sci. Technol.* 18:207–215 (1978).
19. Hermance, C. E., Shinnar, R., and Summerfield, M., *Astronautica Acta* 12:95–112 (1966).
20. Kashiwagi, T., MacDonald, B. W., Isoda, H., and Summerfield, M., *Thirteenth International Symposium on Combustion*, Combustion Institute, Pittsburgh, 1971, pp. 1073–1086.
21. Hermance, C. E., and Kumar, R. K., *AIAA J.* 8:1551–1558 (1970).
22. Kumar, R. K., and Hermance, C. E., *AIAA J.* 9:1615–1620 (1971).
23. Kumar, R. K., and Hermance, C. E., *Combust. Sci. Technol.* 4:191–196 (1972)
24. Kumar, R. K., and Hermance, C. E., *Combust. Sci. Technol.* 14:169–175 (1976).
25. Kindelan, M., and Williams, F. A., *Combust. Sci. Technol.* 16:47–58 (1977).
26. Ritchie, S., Thynell, S., and Kuo, K. K., *J. Prop. Power* 13:367–374 (1997).
27. Melius, C. F., in *Chemistry and Physics of Energetic Materials* (S. Bulusu, Ed.), Kluwer Academic, Norwell, MA, 1990, pp. 21–78.
28. Yetter, R. A., Dryer, F. L., Allen, M. T., and Gatto, J. L., *J. Prop. Power* 11:666–676 (1995).
29. Liau, Y.-C., and Yang, V., *J. Prop. Power* 11:729–739 (1995).
30. Liau, Y.-C., (1996). Ph.D. thesis Department of Mechanical Engineering, The Pennsylvania State University
31. Davidson, J. E., and Beckstead, M. W., *J. Prop. Power* 13:375–383 (1997).
32. Prasad, K., Smooke, M., and Yetter, R. A., *Combust. Flame* 115:406–416 (1998).
33. Miller, M. S., and Anderson, W. R., in *Solid Propellant Chemistry, Combustion, and Motor Interior Ballistics*, Vol. 185 (V. Yang, T. B. Brill, and W. Z., Ren, Eds.), Progress in Astronautics and Aeronautics, AIAA, Reston, VA, 2000, pp. 501–531.
34. Kim, E. S., (2000). Ph.D. thesis Department of Mechanical and Nuclear Engineering, The Pennsylvania State University
35. Chakraboty, D., and Lin M. C., in *Solid Propellant Chemistry, Combustion, and Motor-Interior Ballistics*, Vol. 185, (V. Yang, T. B. Brill, and W. Z., Ren, Eds.), Progress in Astronautics and Aeronautics, AIAA, Reston, VA, 2000, pp. 33–71.
36. Li, S. C., and Williams, F. A., *J. Prop. Power* 12:302–309 (1996).
37. Brill, T. B., Brush, D. G., Patil, D. G., and Chen, J. K., *Twenty-Fourth International Symposium on Combustion, Combustion Institute, Pittsburgh*, 1992, pp. 1907–1914.
38. Thynell, S. T., Gongwer, P. E., and Brill, T. B., *J. Prop. Power* 12:933–939 (1996).
39. Brill, T. B., *J. Prop. Power* 11:740–751 (1995).
40. Lin, C.-Y., Wang, H.-T., Lin, M. C., Melius, C. F., *Int. J. Chemical Kinetics* 22:455–482 (1990).
41. Hanson–Parr, D. M., and Parr, T. P., *J. Energetic Materials* 17:1–47 (1999).
42. Li, S. C., Williams, F. A., and Margolis, S. B., *Combust. Flame* 80:329–349 (1990).
43. Isbell, R. A., and Brewster, M. Q., *Propellants, Explosives, and Pyrotechnics* 23:218–224 (1998).
44. Modest, M. F., *Radiative Heat Transfer*. McGraw-Hill, New York, 1993, pp. 438–449.
45. Kim, E. S., Lee, H. S., Mallery, C. F., and Thynell, S. T., *Combust. Flame* 110:239–255 (1997).
46. Brill, T. B., *Prog. Energy Combust. Sci.* 18:91–116 (1992).
47. Pouchert, C. J., *The Aldrich Library of FT-IR Spectra Vols. 1–3*. Aldrich Chemical Co., Wisconsin, 1997.
48. Isbell, R. A., and Brewster, M. Q., *J. Thermophys. Heat Transfer* 11:65–71 (1997).
49. Kee, R. J., Grcar, J. F., Smooke, M. D., and Miller, J. A., *A Fortran Program for Modeling Steady, Laminar, One-Dimensional, Premixed Flames*. Sandia Report SAND85–8240, Sandia National Laboratories, Albuquerque, NM, 1985.
50. Özisik, M. N., *Boundary Value Problems of Heat Conduction*. International Textbook Company, Scranton, PA, 1968, pp. 427–434.
51. Lutz, A. E., Kee, R. J., and Miller, J. A., *A Fortran Program for Predicting Homogeneous Gas Phase Chemistry Kinetics with Sensitivity Analysis*. Sandia Report SAND87–8248, Sandia National Laboratories, Albuquerque, NM, 1987.
52. Parr, T. P., and Hanson–Parr, D. M., *Twenty-Seventh International Symposium on Combustion*, The Combustion Institute, Pittsburgh, 1998, pp. 2301–2308.

Received 28 November 2000; revised 2 May 2001; accepted 26 May 2001